Article

Structure

Analysis of Global and Site-Specific Radiation Damage in Cryo-EM

Graphical Abstract

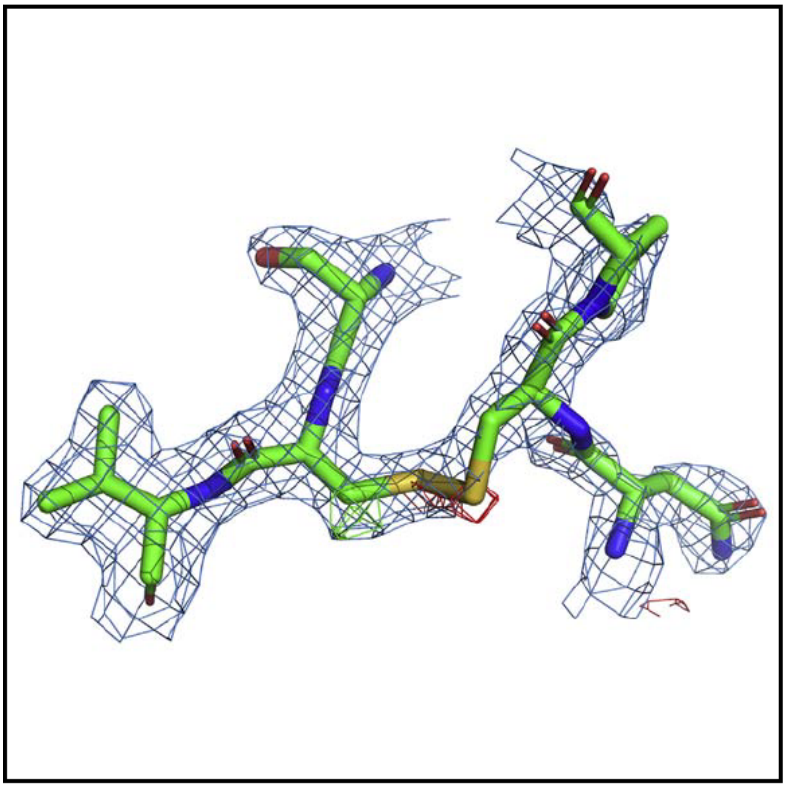

Authors

Johan Hattne, Dan Shi, Calina Glynn, ..., Michael W. Martynowycz, Jose A. Rodriguez, Tamir Gonen

Correspondence

tgonen@ucla.edu

In Brief

The scattered electrons in a cryo-EM measurement provide the information necessary to determine the atomic structure, but inevitably damage the sample. Radiation damage must be controlled to avoid compromising the result. Here, the relationship between exposure and damage is assessed in two different crystalline samples.

Highlights

- Damage to the crystalline order is quantified in reciprocal space
- Site-specific damage to sensitive moieties is assessed in real space
- The effects of damage are particularly pronounced at resolutions better than 3 Å
- At high resolution, damage is apparent at exposures as low as 1 e^{-} $Å^{-2}$

Hattne et al., 2018, Structure *26*, 759–766
May 1, 2018
https://doi.org/10.1016/j.str.2018.03.021

CellPress

Structure
Article

Analysis of Global and Site-Specific Radiation Damage in Cryo-EM

Johan Hattne,[1,2] Dan Shi,[2] Calina Glynn,[3] Chih-Te Zee,[3] Marcus Gallagher-Jones,[3] Michael W. Martynowycz,[1,2] Jose A. Rodriguez,[3] and Tamir Gonen[1,2,4,5,*]
[1]Howard Hughes Medical Institute, University of California, Los Angeles, Los Angeles CA 90095, USA
[2]Janelia Research Campus, Howard Hughes Medical Institute, Ashburn, VA 20147, USA
[3]Department of Chemistry and Biochemistry, UCLA-DOE Institute, University of California, Los Angeles, Los Angeles, CA 90095, USA
[4]Departments of Physiology and Biological Chemistry, David Geffen School of Medicine, University of California, Los Angeles, Los Angeles CA 90095, USA
[5]Lead Contact
*Correspondence: tgonen@ucla.edu
https://doi.org/10.1016/j.str.2018.03.021

SUMMARY

Micro-crystal electron diffraction (MicroED) combines the efficiency of electron scattering with diffraction to allow structure determination from nano-sized crystalline samples in cryoelectron microscopy (cryo-EM). It has been used to solve structures of a diverse set of biomolecules and materials, in some cases to sub-atomic resolution. However, little is known about the damaging effects of the electron beam on samples during such measurements. We assess global and site-specific damage from electron radiation on nanocrystals of proteinase K and of a prion hepta-peptide and find that the dynamics of electron-induced damage follow well-established trends observed in X-ray crystallography. Metal ions are perturbed, disulfide bonds are broken, and acidic side chains are decarboxylated while the diffracted intensities decay exponentially with increasing exposure. A better understanding of radiation damage in MicroED improves our assessment and processing of all types of cryo-EM data.

INTRODUCTION

Structure determination relies on interpreting the outcome of interactions of a beam of quanta with a sample. Most quanta pass through samples without any interaction at all (Henderson, 1995). Other quanta scatter either elastically, whereby they interact with the sample without losing any energy, or inelastically by depositing part of their energy to the sample. In a conventional diffraction measurement, the information that can be gained increases with the number of elastically scattered quanta. Inelastic scattering events manifest as damage, introduce noise, and ultimately limit the signal that can be extracted from the sample.

The success of crystallographic structure determination depends on the ratio of elastic to inelastic scattering events (Nave and Hill, 2005). While this ratio is greater in electron diffraction than in X-ray diffraction (Henderson, 1995), a single incident electron carries sufficient energy to knock out several electrons from an atom in an inelastic scattering event. These ejected, secondary electrons and their associated Auger electrons are mobile even at 77 K (Jones et al., 1987), and can, depending on the chemical composition of the sample and its surrounding mother liquor, cause additional ionization and excitation events in the crystal (Garman, 2010). Further damage from thermal diffusion of atomic and molecular radicals produced by these ionization events is curbed by keeping the sample at cryogenic temperatures, where diffusion is limited (Henderson and Unwin, 1975; Hayward and Glaeser, 1979; Uyeda et al., 1980; Jeng and Chiu, 1984). The absorbed energy, which is related to radiation damage, depends on the chemical composition of the crystal and the medium in which it is embedded, the temperature at which the measurement is performed, and the energy of the incident electrons.

As damage accumulates, its effects become apparent at specific sites as well as throughout the entire crystal. As crystalline order deteriorates, the fraction of unit cells contributing to crystalline diffraction decreases, the B factor generally increases (Kmetko et al., 2006), and the observed unit cell volume may increase as the lattice expands (Ravelli et al., 2002). Consequently, the signal from the obtained diffraction pattern, which varies with the square of the number of scattering unit cells, decreases. To some extent, damage can be compensated for by appropriate scaling procedures (Diederichs, 2006), and may be mitigated in nanocrystals as the probability that secondary electrons escape before causing further damage is higher than in large crystals (Nave and Hill, 2005; Sanishvili et al., 2011).

Site-specific damage may be observed if the impact of radiation damage on the crystal is not uniformly distributed but more selective toward certain moieties (Weik et al., 2000). Unlike global damage, site-specific damage can only be assessed once the dataset has been merged and phased, and a real-space density map is calculated. Site-specific damage becomes apparent when certain bonds are more susceptible to damage than others and may remain invisible if it only occurs in a small fraction of the unit cells or if it is masked by phases calculated from an undamaged model.

Exposure of the sample to the electron beam results in immediate damage even at cryogenic temperatures; low-dose

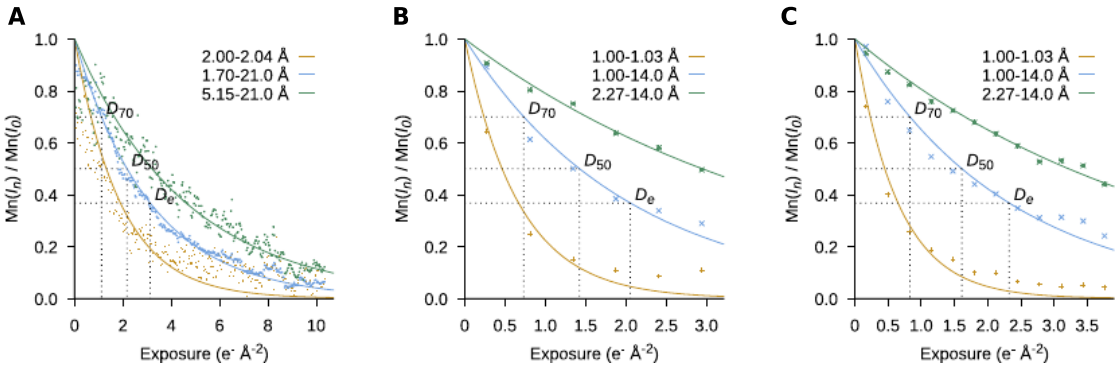

Figure 1. Exposure Dependency of the Mean Intensity of the Unmerged Integrated Reflections

(A–C) Proteinase K (A), the hepta-peptide, GSNQNNF (B), recorded at an exposure rate of 0.0028 e^- Å^{-2} s^{-1}, and GSNQNNF(C) at 0.0017 e^- Å^{-2} s^{-1}. Spots at high resolution fade significantly faster than spots at low resolution. For proteinase K, the electron exposure at which the mean intensity across the entire recorded resolution range is reduced to 70%, 50%, and e^{-1} of its extrapolated value at zero dose is estimated to be D_{70} = 1.1 e^- Å^{-2}, D_{50} = 2.2 e^- Å^{-2}, and D_e = 3.1 e^- Å^{-2}. The corresponding exposures for the 0.0028 e^- Å^{-2} s^{-1} and 0.0017 e^- Å^{-2} s^{-1} peptide datasets are D_{70} = 0.73 e^- Å^{-2}, D_{50} = 1.4 e^- Å^{-2}, and D_e = 2.1 e^- Å^{-2}, and D_{70} = 0.83 e^- Å^{-2}, D_{50} = 1.6 e^- Å^{-2}, and D_e = 2.3 e^- Å^{-2}, respectively.

procedures help minimize the exposure to the sample prior to data recording (Uyeda et al., 1980). Early studies indicated that organic samples deteriorate 4–5× faster at room temperature compared with cryogenic temperatures (Unwin and Henderson, 1975; Hayward and Glaeser, 1979; Jeng and Chiu, 1984). In these studies, two- and/or three-dimensional crystals were used in electron diffraction to look at the overall decay of reflections following exposure to the electron beam. These studies indicated that atomic resolution information (defined as better than 3 Å) was lost after exposure of the sample to only 3 e^- Å^{-2}. In 2013, a new method for cryoelectron microscopy (cryo-EM) was unveiled and termed micro-crystal electron diffraction (MicroED), or three-dimensional electron crystallography of microscopic crystals (Shi et al., 2013; Nannenga et al., 2014b). With continuous rotation MicroED, which is the preferred method of data collection in MicroED, significant loss of diffraction intensity was observed at resolutions better than ~3 Å when only ~3 e^- Å^{-2} were used, consistent with past studies (Hayward and Glaeser, 1979; Jeng and Chiu, 1984; Baker et al., 2010).

Owing to the strong interaction of electrons with matter, and the fact that only diffraction data are collected (no imaging), high-resolution structures can be determined by MicroED from three-dimensional nanocrystals with significantly less total exposure than what is normally used for other cryo-EM modalities. Recent MicroED experiments demonstrated that complete datasets could be collected from a single nanocrystal using a total exposure of less than ~1–2 e^- Å^{-2} (Nannenga et al., 2014a; de la Cruz et al., 2017), making it possible to design new and improved experiments to test for beam-induced damage to the specimen with increasing exposure.

In this study, we set out to determine the damaging effects of electron radiation using MicroED and nanocrystals of a well-characterized sample, proteinase K, and a short hepta-peptide with a bound metal. MicroED data were collected using exposures of 0.0017–0.007 e^- Å^{-2} s^{-1}. Such low exposures allowed us to repeatedly measure the same wedge of reciprocal space from the same crystal and to compare the data obtained over increasing exposure as the experiment progressed. The data were also sufficiently complete to allow us to investigate the effects not only in reciprocal space but also in real space, such that both global and site-specific damage can be observed. The data indicate that beam damage is a limiting factor in high-resolution cryo-EM methods, and the results have implications for all EM methods that use considerably higher exposures for imaging.

RESULTS

Indicators of Global Damage

For both the globular proteinase K and hepta-peptide samples, the overall weakening of the diffraction spots resulting from the loss of crystalline order can be modeled by exponential decay as a function of absorbed dose (Blake and Phillips, 1962; Liebschner et al., 2015) (Figure 1). We note that this model appears to systematically underestimate the intensities of the weakest reflections at high exposures for all samples. This observation does not necessarily invalidate the model: weak reflections are difficult to measure accurately due to noise; to the extent these reflections can be measured at all, they are not discernible by eye. Profiles derived from stronger reflections are likely to overestimate their intensities, and outlier rejection due to, for example, ill-fitting background models, introduces further bias toward more intense reflections.

After an exposure of 1 e^- Å^{-2} the average intensity of all observed reflections in proteinase K decreased to 73% of its extrapolated value at zero dose (Figure 1). After an additional 1.6 e^- Å^{-2}, the high-resolution limit of the data dropped from 1.7 to 1.9 Å (Table 1). Similar trends can be seen in the peptide images at high and low exposure rates where the intensities have dropped to 61% and 65%, respectively, by 1 e^- Å^{-2}. However, the highest-resolution reflections in the peptide data are much stronger than those in proteinase K, and the effect of exposure on optical resolution is consequently not as pronounced. For both peptide datasets, the optical resolution decreases to ~1.1 Å by 2 e^-Å^{-2} (Tables 2 and Table 3).

Table 1. Processing and Refinement Statistics for Proteinase K

Proteinase K	Set 1 (6cl7, EMD-7490)	Set 2 (6cl8, EMD-7491)	Set 3 (6cl9, EMD-7492)	Set 4 (6cla, EMD-7493)	Set 5 (6clb, EMD-7494)
No. of crystals	6	6	6	5	4
$<t_{exp}>$ (s)	123.1	370.0	617.3	862.6	1,107.9
Resolution (Å)	20.74–1.71 (1.74–1.71)	20.78–2.00 (2.05–2.00)	20.81–2.20 (2.27–2.20)	20.87–2.80 (2.95–2.80)	20.92–3.20 (3.46–3.20)
Completeness (%)	93.4 (71.9)	96.9 (97.0)	94.3 (94.6)	88.4 (87.7)	76.8 (77.7)
Multiplicity	6.1 (4.9)	6.2 (6.3)	5.7 (5.8)	5.6 (5.8)	3.3 (3.4)
$CC_{½}$	0.950 (0.164)	0.948 (0.138)	0.925 (0.097)	0.908 (0.142)	0.828 (0.215)
R_{work}/R_{free}	22.13/25.34	21.86/25.88	23.85/30.18	26.30/32.56	21.40/32.62

The average exposure time of a multi-crystal dataset is denoted $<t_{exp}>$; it is defined as the mean cumulative irradiated time of all the frames in the dataset. Numbers in parentheses refer to the highest-resolution shell for refinement. Owing to varying response to radiation, damage-induced non-isomorphism causes the number of datasets that can be merged to decrease at the higher exposures.

The highest-resolution reflections, those providing atomic resolution, are most sensitive to disruption of crystalline order. Consequently, as a result of subtle long-range changes in the lattice, weak, high-resolution reflections fade into the background faster than strong, low-resolution reflections (Blake and Phillips, 1962; Howells et al., 2009), and the highest observable resolution decreases with dose (Tables 1, 2, and 3). In conjunction, fine features in real space density maps disappear at a higher rate than the overall molecular envelope. Generally, high-resolution information, defined as better than 2 Å, was significantly decayed when exposures greater than ~3 e^{-} $Å^{-2}$ were used. Beyond ~4 e^{-} $Å^{-2}$, the reflections at a resolution finer than 2 Å have dropped to 10% of their extrapolated value at zero dose in diffraction patterns of proteinase K. The corresponding exposure for the peptide at high and low dose rates are similar at 2.7 and 3.2 e^{-} $Å^{-2}$, respectively.

As an additional proxy for global damage by electrons we use changes in the relative B factor, B_{rel} (Kmetko et al., 2006), calculated over the reflections in the resolution range common to all datasets of a given sample and exposure rate. For all but the poorest diffracting crystals, B_{rel} increases monotonically with absorbed dose (Figure 2). We also find that the unit cell volume, although a much less reliable indicator of global radiation damage, generally increases with exposure (Murray and Garman, 2002). In our measurements, the unit cell volume of proteinase K increased by a modest 1.8% from 452 to 460 nm^3; the trends for the peptide are much less clear.

Site-Specific Damage

Localized chemical changes within the macromolecule can be analyzed by observing changes in the density attributed to specific atoms in real space. We observe site-specific damage even at exposures as small as 0.1 e^{-} $Å^{-2}$. For example, the presence of positive mF_o-DF_c difference density is detected around the sulfur atoms of the disulfide bonds in proteinase K, indicating that the disulfide bridge was breaking in a significant fraction of the unit cells (Helliwell, 1988), even at total exposure <0.9 e^{-} $Å^{-2}$ (Figure 3). At this exposure, the overall diffraction intensity was reduced to 75% of its extrapolated value at zero dose, indicating that 86% of the unit cells are still diffracting to high resolution (Blake and Phillips, 1962). As the exposure increases, the positive difference density is replaced by negative difference density in the location of the bond and the $2mF_o-DF_c$ density progressively weakens.

We also observe site-specific damage in the decarboxylation of the acidic side chains (Figure 3). Like the disulfide bonds, these moieties have been observed to be particularly sensitive to radiation in both X-ray crystallography (Weik et al., 2000) and single-particle cryo-EM (Bartesaghi et al., 2014; Barad et al., 2015). In proteinase K, the density around the side chains of glutamate and aspartate begins to deteriorate, starting at a

Table 2. Processing and Refinement Statistics for the Hepta-Peptide GSNQNNF at 0.0028 e^{-} $Å^{-2}$ s^{-1}

GSNQNNF (0.0028 e^{-} $Å^{-2}$ s^{-1})	Set 1 (6clc, EMD-7495)	Set 2 (6cld, EMD-7496)	Set 3 (6cle, EMD-7497)	Set 4 (6clf, EMD-7498)	Set 5 (6clg, EMD-7499)	Set 6 (6clh, EMD-7500)
No. of crystals	8	10	9	10	8	6
$<t_{exp}>$ (s)	96.7	289.1	480.1	670.1	860.5	1,050.5
Resolution (Å)	13.96–1.01 (1.03–1.01)	13.95–1.01 (1.03–1.01)	14.04–1.01 (1.03–1.01)	13.98–1.15 (1.20–1.15)	13.75–1.35 (1.44–1.35)	13.96–1.37 (1.46–1.37)
Completeness (%)	76.6 (67.0)	82.4 (57.2)	77.2 (37.6)	81.2 (82.9)	77.2 (78.1)	73.5 (74.1)
Multiplicity	5.9 (5.4)	6.4 (4.5)	5.7 (3.1)	6.5 (6.0)	5.8 (5.8)	4.7 (4.5)
$CC_{1/2}$	0.980 (0.892)	0.983 (0.842)	0.988 (0.758)	0.986 (0.850)	0.986 (0.590)	0.968 (0.385)
R_{work}/R_{free}	17.77/15.86	22.03/21.31	24.52/24.38	26.59/29.28	21.95/26.86	22.50/29.75

Rows as per Table 1.

Table 3. Processing and Refinement Statistics for the Hepta-Peptide GSNQNNF at 0.0017 e⁻ Å⁻² s⁻¹

GSNQNNF (0.0017 e^{-} $Å^{-2}$ s^{-1})	Set 1 (6cli, EMD-7501)	Set 2 (6clj, EMD-7502)	Set 3 (6clk, EMD-7503)	Set 4 (6cll, EMD-7504)	Set 5 (6clm, EMD-7505)	Set 6 (6cln, EMD-7506)	Set 7 (6clo, EMD-7507)	Set 8 (6clp, EMD-7508)	Set 9 (6clq, EMD-7509)	Set 10 (6clr, EMD-7510)	Set 11 (6cls; EMD-7511)	Set 12 (6clt; EMD-7512)
No. of crystals	11	11	9	10	11	9	11	10	12	10	10	9
$<t_{exp}>$ (s)	97.2	291.3	484.6	677.1	869.0	1,060.6	1,251.0	1,442.9	1,636.2	1,832.2	2,024.3	2,214.0
Resolution (Å)	14.00–1.01 (1.03–1.01)	13.96–1.01 (1.03–1.01)	13.92–1.01 (1.03–1.01)	11.39–1.02 (1.03–1.02)	13.93–1.01 (1.03–1.01)	13.87–1.15 (1.03–1.15)	13.76–1.15 (1.20–1.15)	13.79–1.16 (1.20–1.16)	13.79–1.21 (1.26–1.21)	13.77–1.31 (1.38–1.31)	13.73–1.46 (1.57–1.46)	13.73–1.45 (1.59–1.45)
Completeness (%)	78.0 (61.6)	79.6 (74.0)	80.0 (74.9)	72.5 (64.8)	78.1 (66.3)	79.7 (82.6)	78.8 (79.6)	76.0 (78.9)	79.3 (77.9)	79.4 (80.3)	78.7 (80.0)	77.6 (77.7)
Multiplicity	7.6 (6.1)	7.8 (6.0)	6.4 (4.3)	7.4 (5.2)	7.4 (4.5)	5.8 (6.2)	7.1 (6.9)	6.9 (6.7)	7.9 (7.2)	6.7 (5.8)	6.8 (7.2)	6.0 (6.5)
$CC_{1/2}$	0.972 (0.825)	0.973 (0.809)	0.948 (0.544)	0.895 (0.402)	0.978 (0.521)	0.940 (0.750)	0.917 (0.634)	0.988 (0.626)	0.974 (0.731)	0.960 (0.619)	0.980 (0.596)	0.984 (0.736)
R_{work}/R_{free}	19.12/ 19.62	20.51/ 19.60	26.05/ 26.74	24.64/ 27.98	22.90/ 25.54	21.66/ 22.12	26.55/ 26.79	23.92/ 27.72	23.60/ 26.17	24.07/ 28.79	22.31/ 33.71	22.01/ 30.73

Rows as per Table 1.

total exposure of ~2 e^{-} $Å^{-2}$, and completely disappears after approximately 5 e^{-} $Å^{-2}$ (Figure 3).

The peptide unit cell contains a zinc atom, which displays significant signs of site-specific radiation damage at exposures >0.8 e^{-} $Å^{-2}$ (Figure 4). For the bound zinc, the radiation damage is primarily modeled using the atomic displacement parameter (ADP). Unlike occupancies, which model large-scale discrete disorder and were fixed at unity in all models, the ADPs describe harmonic vibrations around the mean position of the atoms. While the density around the zinc atom in the model remains positive even at the highest exposure, its ADP generally increases with exposure (Figure 4). The displacement begins with as little total exposure as 0.2 e^{-} $Å^{-2}$, when the ADP of the zinc is 1.3× higher than the average ADP in the peptide model.

Site specific damage was further assessed in real space using RIDL (Bury et al., 2015), which calculates the maximum density loss D_{loss} for each atom in the model. This provides a means to objectively establish the sensitivity of different amino acids to electron radiation. Generally, the results from MicroED are consistent with the order and appearance of site-specific damage observed in X-ray crystallography: metals are significantly more prone to damage, and glutamate, aspartate, and cysteine residues accumulate damage even at very low electron beam exposures (Figure 5).

DISCUSSION

Past studies of radiation damage in cryo-EM described the exposure-dependent decay of diffraction intensities up to and including 3 Å resolution (Henderson and Unwin, 1975; Hayward and Glaeser, 1979; Jeng and Chiu, 1984; Baker et al., 2010). No data were analyzed at resolutions better than 3 Å, likely because such data were not recorded at the time. Unfortunately, even a recent study that reported a 2.6 Å resolution single-particle reconstruction included an analysis of beam-induced damage only to lower resolution (Grant and Grigorieff, 2015). Moreover, while the early experiments analyzed the decay of diffraction intensities, little or no analysis of the effects of exposure on real space was described. This is likely because the effects of specific damage in real space are difficult to characterize to any degree of accuracy at low resolution.

We performed a deep analysis of the effects of electron radiation damage on biological samples at resolutions better than 1 Å using MicroED (Shi et al., 2013; Nannenga et al., 2014b). Using ultra-low exposures allowed us to collect sufficient data from several crystals for structure determination. Each crystal was then sequentially exposed to the electron beam and additional structures were determined, from the very same crystals, at increasing levels of total exposure. In this way, we could investigate the effects of exposure on both reciprocal and real space informing us on both global and site-specific damage to the sample. With this approach, we could follow the trends of beam-induced damage in biological matter at very high resolutions (better than 1 Å) in a way not previously possible in cryo-EM.

Our real-space analysis shows that site-specific damage is apparent at high resolution, even with exposures less than 1 e^{-} $Å^{-2}$; these exposures are well below those currently used in other cryo-EM modalities, for example imaging in single-particle EM. This analysis therefore holds important

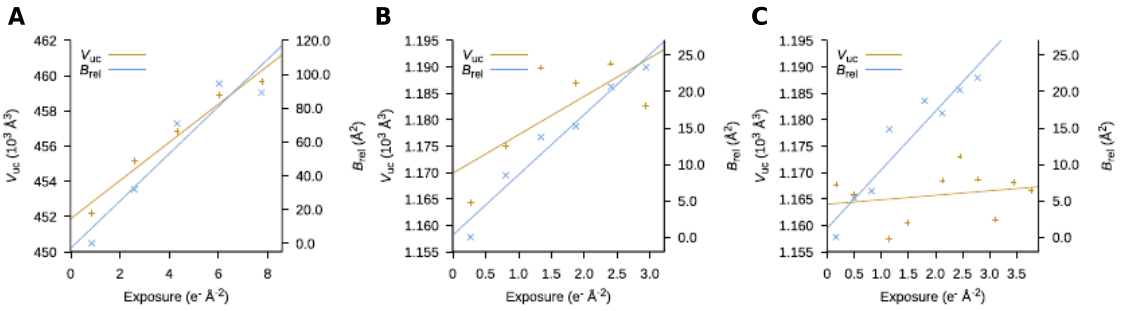

Figure 2. Exposure Dependency of the Unit Cell Volume, V_{uc}, and Relative B Factor, B_{rel}

V_{uc} and B_{rel} were averaged across all the crystals at each exposure. For B_{rel} only reflections in a sufficiently large resolution range common to all datasets were considered (20.8–3.20 Å for proteinase K; 14.0–1.2 Å for GSNQNNF). (A) proteinase K, (B) the hepta-peptide, GSNQNNF, recorded at an exposure rate of 0.0028 e$^-$ Å^{-2} s^{-1}, and (C) GSNQNNF at 0.0017 e$^-$ Å^{-2} s^{-1}.

implications for all cryo-EM methods, particularly single-particle EM, as resolutions that approach those commonly observed in crystallography have recently been reported (Merk et al., 2016).

Imaging in single-particle cryo-EM allows the determination of protein structures from a collection of thousands of projection images of individual particles oriented randomly in vitrified ice. When a sufficiently fast camera is available, single-particle cryo-EM data are often collected as movie. The exposure delivered to the sample reflects a trade-off between contrast and loss of high-resolution information to radiation damage. Using catalase crystals, it was previously suggested that the optimal trade-off between signal and damage was ~20 e$^-$ Å^{-2} for the target resolution of 20 Å, while for 3 Å resolution it was recommended that 10 e$^-$ Å^{-2} be used (Baker et al., 2010). In single particle EM, the total exposure that is typically more than 20 e$^-$ Å^{-2}, is fractionated over a sequence of short exposures. This allows individual frames to be corrected for specimen drift and beam-induced movement prior to averaging, while the first frame is usually discarded during processing. The last frames aid alignment but are excluded from the final average because they contribute little high-resolution information. The average of the first ~2–5 frames from the movie therefore reflect a superposition of the same particles exposed to electron doses in the range of 2–10 e$^-$ Å^{-2}, and these are used for the final reconstruction when combined with data from thousands of other particles.

Since the damage mechanisms in all these EM methods originate from the same phenomena, it is likely that the effects of

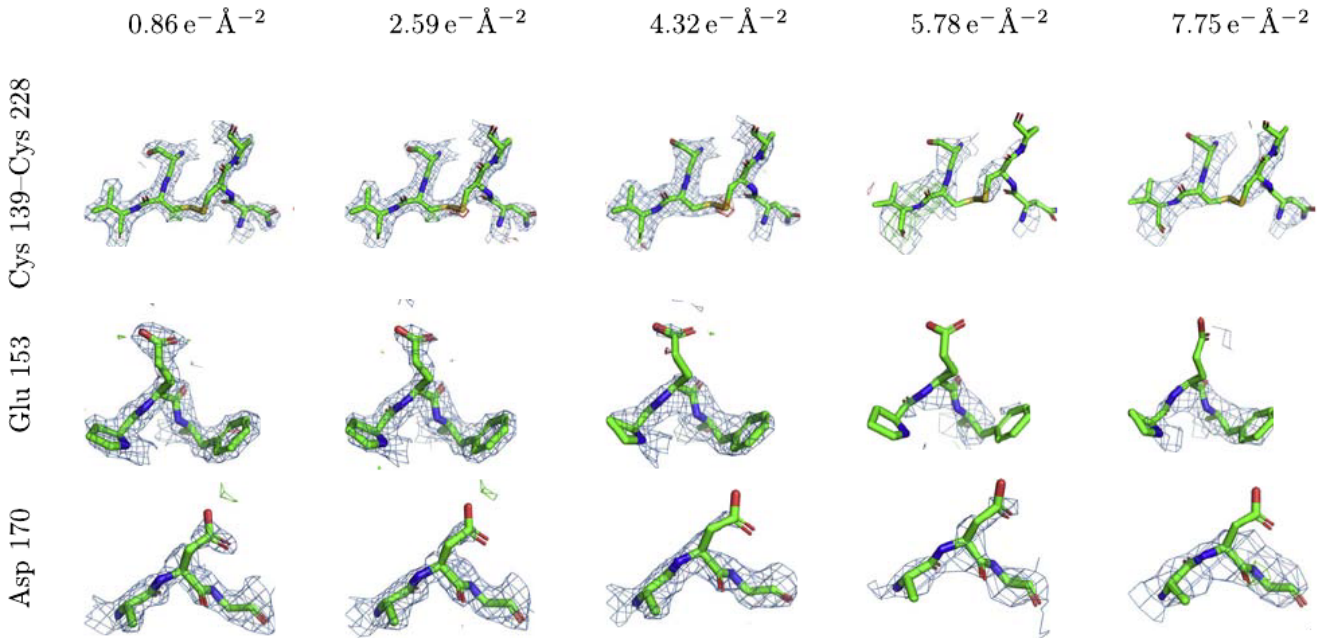

Figure 3. Disulfide Bond Breakage and Decarboxylation of Acidic Side Chains Indicate Site-Specific Radiation Damage in Proteinase K

$2mF_o-DF_c$ maps (blue meshes) are contoured at 1.5σ above the mean, mF_o-DF_c difference densities (green/red meshes) are contoured at ±3σ above/below the mean. Maps up to and including those calculated at 4.3 e$^-$ Å^{-2} use data extending to 2.2 Å; the two maps at the highest exposure only use reflections up to 3.2 Å. Densities are carved to 2 Å around the selected atoms. All figures were generated using PyMol (Schrödinger, 2014).

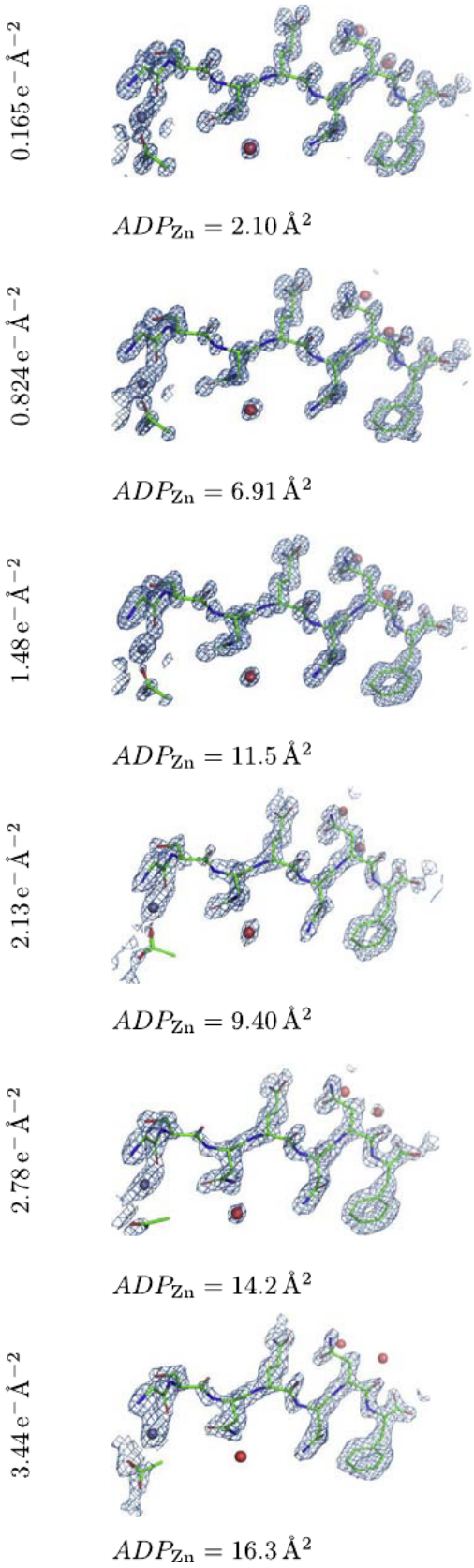

Figure 4. Exposure Dependency on the Hepta-Peptide Density

$2mF_o–DF_c$ (blue meshes, contoured at 1.5σ above the mean) and $mF_o–DF_c$ density (red/green meshes, contoured at ±3σ above/below the mean) from the GSNQNNF hetpa-peptide at 0.0017 e^- Å^{-2} s^{-1}. All densities are carved to 2 Å around the model and the maps at electron exposures up to and including 1.5 e^- Å^{-2} are calculated using all observed reflections to 1.01 Å; remaining maps use reflections up to 1.45 Å. The atomic displacement parameter of the Zn atom, ADP_{Zn} (purple sphere to the left), generally increases over the course of exposure.

randomly distributed damage events are washed out during the immense averaging and the use of methods to exclude certain particles from the final reconstruction in single-particle EM. However, site-specific damage to acidic side chains has already been observed at 3.2 Å in 10 e^- Å^{-2} exposures (Bartesaghi et al., 2014). We surmise that the underlying damage to the sample may limit the attainable resolution in single-particle cryo-EM at the doses currently used (Grant and Grigorieff, 2015; Merk et al., 2016), and that with such exposure levels the collected data are of damaged particles. When known structures are reconstructed by single-particle EM, even if the resulting map is noisy because of damage, it can still be readily interpreted because the correct answer is available. But for novel structures, where the correct structure is unknown, building structures *de novo* with noisy maps of damaged protein is very challenging and could be prohibitive.

Quantification of radiation damage and estimates of crystal lifetime under irradiation not only depend on the sample (e.g., the number of scattering unit cells and their size, composition and thickness of the surrounding mother liquor and the embedding vitrified ice), and the measurement setup (e.g., quanta, dose, and temperature), but also on how data were processed and analyzed. Measures such as the upper resolution limit, B factors, and unit cell volume are often the result of some optimization procedure and may be affected by factors other than the actual damage to the crystal (Kmetko et al., 2006). This is reflected in the literature by the wide spread of dose limits. The D_{50} value of 2.2 e^- Å^{-2} calculated from reflections of proteinase K in the 21.0–1.7 Å interval is consistent with past measurements using electron diffraction from two-dimensional crystals (Stark et al., 1996) as well as three-dimensional crystals (Unwin and Henderson, 1975; Jeng and Chiu, 1984; Baker et al., 2010). When D_{50} was calculated from the reflections in the 14.0–1.7 Å interval of the much smaller hepta-peptide, its value was 2.0 and 2.2 e^- Å^{-2} for high and low exposure rates, respectively, very close to the value obtained from proteinase K. In line with previous studies in synchrotron X-ray crystallography at comparable flux densities and temperatures, we do not see any effects from the dose rate on the observed global damage (Holton, 2009; Warkentin et al., 2013).

Given that the absorbed dose will ultimately limit the amount of meaningful data that can be extracted from a sample, data collection in the face of radiation damage may be viewed as an optimization problem. The more electrons are delivered to the sample in cryo-EM the stronger the signal, but then noise and damage accumulate and the high-resolution information suffers. Where each sample need only be exposed once, e.g., single-particle cryo-EM or serial femtosecond crystallography (Schlichting, 2015), the exposure can be tuned to maximize the signal-to-noise ratio. When pictures are recorded in

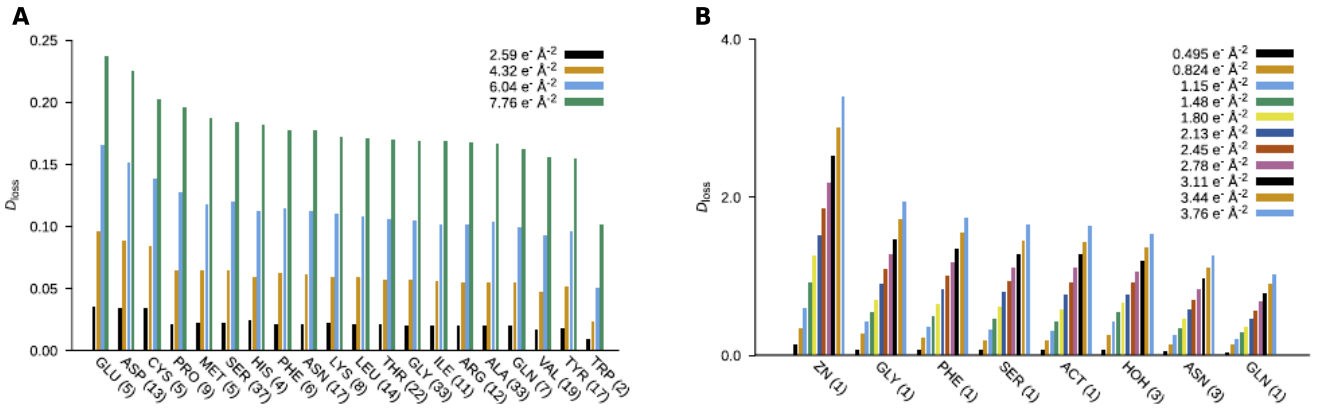

Figure 5. Accumulated Density Loss

(A and B) Density loss in arbitrary units for all the amino acids, ligands, and ions present in the refined models of (A) proteinase K and (B) the hepta-peptide. The entities are sorted in the approximate order of damage onset. The numbers in parentheses denote the occurrence of the respective amino acid in the structure. Only reflections in the resolution range common to all datasets are considered (20.8–3.20 Å for proteinase K; 14.0–1.45 Å for GSNQNNF).

cryo-EM a minimum level of exposure is required so that sufficient signal is recorded on the camera to facilitate phase contrast and faithful reconstructions. This need for phase contrast makes it hard to lower the total dose in these experiments where it was recommended to use 10 e^{-} $Å^{-2}$ for optimal trade-off between signal and noise for the target resolution of only 3 Å (Baker et al., 2010).

In MicroED, where phases are lost and only amplitudes are recorded, the minimum exposure necessary for recording the signal is significantly lower than in single-particle EM. This allows data collection at extremely low exposures <0.01 e^{-} $Å^{-2}$ s^{-1} and entire datasets to be collected from a total exposure less than a single electron per $Å^2$ at which point atomic resolution information can be preserved. Our estimated D_{50} rate of approximately 2 e^{-} $Å^{-2}$ sets an upper target for single-particle cryo-EM experiments seeking to maximize resolution. This is particularly challenging, but with increasingly sensitive cameras and better algorithms to allow the use of the first few frames of the recorded movies one might be able to achieve such a feat.

STAR★METHODS

Detailed methods are provided in the online version of this paper and include the following:

- KEY RESOURCES TABLE
- CONTACT FOR REAGENT AND RESOURCE SHARING
- METHOD DETAILS
  - Proteinase K
  - GSNQNNF
- QUANTIFICATION AND STATISTICAL ANALYSIS
- DATA AND SOFTWARE AVAILABILITY

ACKNOWLEDGMENTS

The Gonen laboratory is supported by funds from the Howard Hughes Medical Institute. J.A.R. is partly supported by NSF grant no. DMR 1548924, DOE grant DE-FC02-02ER63421, and as a Searle Scholar and a Beckman Young Investigator. M.G.J. is supported by a QCB Collaboratory Postdoctoral Fellowship.

AUTHOR CONTRIBUTIONS

Conceptualization, J.A.R. and T.G.; Investigation, D.S., C.G., and C.-T.Z.; Formal Analysis, J.H., C.-T.Z, M.G.-J., and M.W.M.; Writing, J.H., D.S., J.A.R., and T.G.

DECLARATION OF INTERESTS

The authors declare no competing interests.

Received: December 9, 2017
Revised: February 1, 2018
Accepted: March 30, 2018
Published: April 26, 2018

REFERENCES

Baker, L.A., Smith, E.A., Bueler, S.A., and Rubinstein, J.L. (2010). The resolution dependence of optimal exposures in liquid nitrogen temperature electron cryomicroscopy of catalase crystals. J. Struct. Biol. *169*, 431–437.

Barad, B.A., Echols, N., Wang, R.Y.R., Cheng, Y., Dimaio, F., Adams, P.D., and Fraser, J.S. (2015). EMRinger: side chain-directed model and map validation for 3D cryo-electron microscopy. Nat. Methods *12*, 943–946.

Bartesaghi, A., Matthies, D., Banerjee, S., Merk, A., and Subramaniam, S. (2014). Structure of -galactosidase at 3.2-A resolution obtained by cryo-electron microscopy. Proc. Natl. Acad. Sci. USA *111*, 11709–11714.

Battye, T.G.G., Kontogiannis, L., Johnson, O., Powell, H.R., and Leslie, A.G.W. (2011). iMOSFLM: a new graphical interface for diffraction-image processing with MOSFLM. Acta Crystallogr.D Biol. Crystallogr. *67* (Pt 4), 271–281.

Blake, C.C.F., and Phillips, D.C. (1962). Effects of X-irradiation on Single Crystals of Myoglobin (The Royal Institution), pp. 183–191.

Bury, C., Garman, E.F., Ginn, H.M., Ravelli, R.B.G., Carmichael, I., Kneale, G., and McGeehan, J.E. (2015). Radiation damage to nucleoprotein complexes in macromolecular crystallography. J. Synchrotron Radiat. *22*, 213–224.

de la Cruz, M.J., Hattne, J., Shi, D., Seidler, P., Rodriguez, J., Reyes, F.E., Sawaya, M.R., Cascio, D., Weiss, S.C., Kim, S.K., et al. (2017). Atomic-resolution structures from fragmented protein crystals with the cryoEM method MicroED. Nat. Methods *14*, 399–402.

Diederichs, K. (2006). Some aspects of quantitative analysis and correction of radiation damage. Acta Crystallogr. D Biol. Crystallogr. *62*, 96–101.

Evans, P.R., and Murshudov, G.N. (2013). How good are my data and what is the resolution? Acta Crystallogr. D Biol. Crystallogr. *69*, 1204–1214.

Garman, E.F. (2010). Radiation damage in macromolecular crystallography: what is it and why should we care? Acta Crystallogr. D Biol. Crystallogr. *66*, 339–351.

Grant, T., and Grigorieff, N. (2015). Measuring the optimal exposure for single particle cryo-EM using a 2.6 Å reconstruction of rotavirus VP6. Elife *4*, https://doi.org/10.7554/eLife.06980.

Hattne, J., Reyes, F.E., Nannenga, B.L., Shi, D., de la Cruz, M.J., Leslie, A.G.W., and Gonen, T. (2015). MicroED data collection and processing. Acta Crystallogr. A Found. Adv. *71*, 353–360.

Hattne, J., Shi, D., de la Cruz, M.J., Reyes, F.E., and Gonen, T. (2016). Modeling truncated pixel values of faint reflections in MicroED images. J. Appl. Crystallogr. *49*, 1029–1034.

Hayward, S.B., and Glaeser, R.M. (1979). Radiation damage of purple membrane at low temperature. Ultramicroscopy *4*, 201–210.

Helliwell, J.R. (1988). Protein crystal perfection and the nature of radiation damage. J. Cryst. Growth *90*, 259–272.

Henderson, R. (1995). The potential and limitations of neutrons, electrons and X-rays for atomic resolution microscopy of unstained biological molecules. Q. Rev. Biophys. *28*, 171–193.

Henderson, R., and Unwin, P.N. (1975). Three-dimensional model of purple membrane obtained by electron microscopy. Nature *257*, 28–32.

Holton, J.M. (2009). A beginner's guide to radiation damage. J. Synchrotron Radiat. *16* (Pt 2), 133–142.

Howell, P.L., and Smith, G.D. (1992). Identification of heavy-atom derivatives by normal probability methods. J. Appl. Crystallogr. *25*, 81–86.

Howells, M.R., Beetz, T., Chapman, H.N., Cui, C., Holton, J.M., Jacobsen, C.J., Kirz, J., Lima, E., Marchesini, S., Miao, H., et al. (2009). An assessment of the resolution limitation due to radiation-damage in X-ray diffraction microscopy. J. Electron Spectrosc. Relat. Phenom. *170*, 4–12.

Jeng, T.-W., and Chiu, W. (1984). Quantitative assessment of radiation damage in a thin protein crystal. J. Microsc. *136*, 35–44.

Jones, G.D.D., Lea, J.S., Symons, M.C.R., and Taiwo, F.A. (1987). Structure and mobility of electron gain and loss centres in proteins. Nature *330*, 772–773.

Kabsch, W. (2010a). Integration, scaling, space-group assignment and post-refinement. Acta Crystallogr. D Biol. Crystallogr. *66* (Pt 2), 133–144.

Kabsch, W. (2010b). XDS. Acta Crystallogr. D Biol. Crystallogr. *66* (Pt 2), 125–132.

Kmetko, J., Husseini, N.S., Naides, M., Kalinin, Y., and Thorne, R.E. (2006). Quantifying X-ray radiation damage in protein crystals at cryogenic temperatures. Acta Crystallogr. D Biol. Crystallogr. *62* (Pt 9), 1030–1038.

Leslie, A.G.W., and Powell, H.R. (2007). Processing diffraction data with mosflm. In Evolving Methods for Macromolecular Crystallography (NATO Science Series II: Mathematics, Physics and Chemistry), R.J. Read and J.L. Sussman, eds. (Springer), pp. 41–51.

Liebschner, D., Rosenbaum, G., Dauter, M., and Dauter, Z. (2015). Radiation decay of thaumatin crystals at three X-ray energies. Acta Crystallogr. D Biol. Crystallogr. *71*, 772–778.

Martynowycz, M., Glynn, C., Miao, J., de la Cruz, M.J., Hattne, J., Shi, D., Cascio, D., Rodriguez, J., and Gonen, T. (2017). MicroED structures from micrometer thick protein crystals. bioRχiv. https://doi.org/10.1101/152504.

Merk, A., Bartesaghi, A., Banerjee, S., Falconieri, V., Rao, P., Davis, M.I., Pragani, R., Boxer, M.B., Earl, L.A., Milne, J.L.S., and Subramaniam, S. (2016). Breaking cryo-EM resolution barriers to facilitate drug discovery. Cell *165*, 1698–1707.

Murray, J., and Garman, E. (2002). Investigation of possible free-radical scavengers and metrics for radiation damage in protein cryocrystallography. J. Synchrotron Radiat. *9*, 347–354.

Murshudov, G.N., Skubák, P., Lebedev, A.A., Pannu, N.S., Steiner, R.A., Nicholls, R.A., Winn, M.D., Long, F., and Vagin, A.A. (2011). REFMAC5 for the refinement of macromolecular crystal structures. Acta Crystallogr. D Biol. Crystallogr. *67* (Pt 4), 355–367.

Nannenga, B.L., Shi, D., Hattne, J., Reyes, F.E., and Gonen, T. (2014a). Structure of catalase determined by MicroED. Elife *3*, e03600.

Nannenga, B.L., Shi, D., Leslie, A.G.W., and Gonen, T. (2014b). High-resolution structure determination by continuous-rotation data collection in MicroED. Nat. Methods *11*, 927–930.

Nave, C., and Hill, M.A. (2005). Will reduced radiation damage occur with very small crystals? J. Synchrotron Radiat. *12* (Pt 3), 299–303.

Oliphant, T.E. (2007). Python for scientific computing. Comput. Sci. Eng. *9*, 10–20.

Ravelli, R.B.G., Theveneau, P., McSweeney, S., and Caffrey, M. (2002). Unit-cell volume change as a metric of radiation damage in crystals of macromolecules. J. Synchrotron Radiat. *9*, 355–360.

Sanishvili, R., Yoder, D.W., Pothineni, S.B., Rosenbaum, G., Xu, S., Vogt, S., Stepanov, S., Makarov, O.A., Corcoran, S., Benn, R., et al. (2011). Radiation damage in protein crystals is reduced with a micron-sized X-ray beam. Proc. Natl. Acad.Sci. USA *108*, 6127–6132.

Schlichting, I. (2015). Serial femtosecond crystallography: the first five years. IUCrJ *2*, 246–255.

Schrödinger, L.L.C. (2014). The PyMOL Molecular Graphics System (Schrödinger), Available at: https://www.pymol.org

Sheldrick, G.M. (2008). A short history of SHELX. Acta Crystallogr. A Found. Crystallogr. *64* (Pt 1), 112–122.

Shi, D., Nannenga, B.L., Iadanza, M.G., and Gonen, T. (2013). Three-dimensional electron crystallography of protein microcrystals. Elife *2*, e01345.

Shi, D., Nannenga, B.L., de la Cruz, M.J., Liu, J., Sawtelle, S., Calero, G., Reyes, F.E., Hattne, J., and Gonen, T. (2016). The collection of MicroED data for macromolecular crystallography. Nat. Protoc. *11*, 895–904.

Stark, H., Zemlin, F., and Boettcher, C. (1996). Electron radiation damage to protein crystals of bacteriorhodopsin at different temperatures. Ultramicroscopy *63*, 75–79.

Unwin, P.N.T., and Henderson, R. (1975). Molecular structure determination by electron microscopy of unstained crystalline specimens. J. Mol. Biol. *94*, 425–440.

Urzhumtseva, L.M., Klaholz, B., and Urzhumtsev, A.G. (2013). On effective and optical resolutions of diffraction data sets. Acta Crystallogr. D Biol. Crystallogr. *69* (Pt 10), 1921–1934.

Uyeda, N., Kobayashi, T., Ishizuka, K., and Fujiyoshi, Y. (1980). Crystal structure of Ag·TCNQ. Nature *285*, 95–97.

Vagin, A., and Teplyakov, A. (1997). MOLREP: an automated program for molecular replacement. J. Appl. Crystallogr. *30*, 1022–1025.

Warkentin, M., Hopkins, J.B., Badeau, R., Mulichak, A.M., Keefe, L.J., and Thorne, R.E. (2013). Global radiation damage: temperature dependence, time dependence and how to outrun it. J. Synchrotron Radiat. *20* (Pt 1), 7–13.

Weik, M., Ravelli, R.B.G., Kryger, G., McSweeney, S., Raves, M.L., Harel, M., Gros, P., Silman, I., Kroon, J., and Sussman, J.L. (2000). Specific chemical and structural damage to proteins produced by synchrotron radiation. Proc. Natl. Acad. Sci. USA *97*, 623–628.

Winn, M.D., Ballard, C.C., Cowtan, K.D., Dodson, E.J., Emsley, P., Evans, P.R., Keegan, R.M., Krissinel, E.B.E.B., McCoy, A.J., McNicholas, S.J., et al. (2011). Overview of the CCP4 suite and current developments. Acta Crystallogr. D Biol. Crystallogr. *67* (Pt 4), 235–242.

STAR★METHODS

KEY RESOURCES TABLE

REAGENT or RESOURCE	SOURCE	IDENTIFIER
Chemicals, Peptides, and Recombinant Proteins		
Proteinase K	Sigma-Aldrich	Cat#P2308; CAS: 39450-01-6
Ammonium sulfate	Sigma-Aldrich	Cat#A4418; CAS: 7783-20-2
BIS-TRIS	Sigma-Aldrich	Cat#B9754; CAS: 6976-37-0
GSNQNNF	GenScript	N/A
Polyethylene glycol 8,000	Hampton Research	Cat#HR2-535; CAS: 25322-68-3
MES sodium salt	Sigma-Aldrich	Cat#M3885; CAS: 71119-23-8
Zinc acetate dihydrate	Sigma-Aldrich	Cat#96459; CAS: 5970-45-6
Deposited Data		
Atomic coordinates, proteinase K crystal structure	(Hattne et al., 2016)	PDB: 5i9s
Atomic coordinates and density map of proteinase K at 0.86 e^{-} $Å^{-2}$	this paper	PDB: 6cl7; EMDB: EMD-7490
Atomic coordinates and density map of proteinase K at 2.6 e^{-} $Å^{-2}$	this paper	PDB: 6cl8; EMDB: EMD-7491
Atomic coordinates and density map of proteinase K at 4.3 e^{-} $Å^{-2}$	this paper	PDB: 6cl9; EMDB: EMD-7492
Atomic coordinates and density map of proteinase K at 6.0 e^{-} $Å^{-2}$	this paper	PDB: 6cla; EMDB: EMD-7493
Atomic coordinates and density map of proteinase K at 7.8 e^{-} $Å^{-2}$	this paper	PDB: 6clb; EMDB: EMD-7494
Atomic coordinates and density map of GSQNNF at 0.27 e^{-} $Å^{-2}$	this paper	PDB: 6clc; EMDB: EMD-7495
Atomic coordinates and density map of GSQNNF at 0.81 e^{-} $Å^{-2}$	this paper	PDB: 6cld; EMDB: EMD-7496
Atomic coordinates and density map of GSQNNF at 1.3 e^{-} $Å^{-2}$	this paper	PDB: 6cle; EMDB: EMD-7497
Atomic coordinates and density map of GSQNNF at 1.9 e^{-} $Å^{-2}$	this paper	PDB: 6clf; EMDB: EMD-7498
Atomic coordinates and density map of GSQNNF at 2.4 e^{-} $Å^{-2}$	this paper	PDB: 6clg; EMDB: EMD-7499
Atomic coordinates and density map of GSQNNF at 2.9 e^{-} $Å^{-2}$	this paper	PDB: 6clh; EMDB: EMD-7500
Atomic coordinates and density map of GSQNNF at 0.17 e^{-} $Å^{-2}$	this paper	PDB: 6cli; EMDB: EMD-7501
Atomic coordinates and density map of GSQNNF at 0.50 e^{-} $Å^{-2}$	this paper	PDB: 6clj; EMDB: EMD-7502
Atomic coordinates and density map of GSQNNF at 0.82 e^{-} $Å^{-2}$	this paper	PDB: 6clk; EMDB: EMD-7503
Atomic coordinates and density map of GSQNNF at 1.2 e^{-} $Å^{-2}$	this paper	PDB: 6cll; EMDB: EMD-7504
Atomic coordinates and density map of GSQNNF at 1.5 e^{-} $Å^{-2}$	this paper	PDB: 6clm; EMDB: EMD-7505
Atomic coordinates and density map of GSQNNF at 1.8 e^{-} $Å^{-2}$	this paper	PDB: 6cln; EMDB: EMD-7506
Atomic coordinates and density map of GSQNNF at 2.1 e^{-} $Å^{-2}$	this paper	PDB: 6clo; EMDB: EMD-7507
Atomic coordinates and density map of GSQNNF at 2.5 e^{-} $Å^{-2}$	this paper	PDB: 6clp; EMDB: EMD-7508

(*Continued on next page*)

Continued		
REAGENT or RESOURCE	SOURCE	IDENTIFIER
Atomic coordinates and density map of GSQNNF at 2.8 e^{-} Å^{-2}	this paper	PDB: 6clq; EMDB: EMD-7509
Atomic coordinates and density map of GSQNNF at 3.1 e^{-} Å^{-2}	this paper	PDB: 6clr; EMDB: EMD-7510
Atomic coordinates and density map of GSQNNF at 3.4 e^{-} Å^{-2}	this paper	PDB: 6cls; EMDB: EMD-7511
Atomic coordinates and density map of GSQNNF at 3.8 e^{-} Å^{-2}	this paper	PDB: 6clt; EMDB: EMD-7512
Software and Algorithms		
TVIPS tools	(Hattne et al., 2015)	N/A
iMosflm	(Leslie and Powell, 2007; Battye et al., 2011)	RRID:SCR_014217
AIMLESS	(Evans and Murshudov, 2013)	RRID:SCR_015747
MOLREP	(Vagin and Teplyakov, 1997)	RRID:SCR_007255
XDS	(Kabsch, 2010b)	RRID:SCR_015652
XSCALE	(Kabsch, 2010a)	RRID:SCR_015652
XDSCONV	(Kabsch, 2010b)	RRID:SCR_015652
SHELXD	(Sheldrick, 2008)	RRID:SCR_014220
SCALEIT	(Howell and Smith, 1992)	RRID:SCR_007255
EFRESOL	(Urzhumtseva et al., 2013)	N/A
REFMAC	(Murshudov et al., 2011)	RRID:SCR_014225
AREAIMOL	(Winn et al., 2011)	RRID:SCR_007255
RIDL	(Bury et al., 2015)	N/A
PyMol	(Schrödinger, 2014)	RRID:SCR_000305
Other		
TEM grids	Quantifoil	N/A
easiGlow glow discharge cleaning system	PELCO	N/A
Vitrobot Mark IV plunge-freezer	Thermo Fisher	N/A
Gatan 626 cryo-transfer holder	Gatan	N/A
FEI Tecnai F20	Thermo Fischer	N/A
TemCam-F416	TVIPS	N/A

CONTACT FOR REAGENT AND RESOURCE SHARING

Further information and requests for resources and reagents should be directed to and will be fulfilled by the lead contact, Tamir Gonen (tgonen@ucla.edu).

METHOD DETAILS

Proteinase K

Crystal Growth

Proteinase K from *Engyodontium album* (Sigma-Aldrich, St Louis, MO, USA) was prepared by combining 2 ml of protein solution (50 mg ml^{-1}) with 2 ml of precipitant solution (1.0–1.3 M ammonium sulfate, 0.1 M Tris pH 8.0) (Hattne et al., 2016).

Sample Preparation

The protein solution was dispensed on a glow-discharged grid (easiGlow; Pelco) and vitrified with force position 24 in an FEI (now Thermo Fisher) Vitrobot Mark IV after blotting for 12 s at an environment humidity of 30% (Shi et al., 2016). Frozen-hydrated grids were loaded onto a Gatan 626 cryo-holder and transferred to the microscope, where the specimen temperature was maintained at ~100 K.

Data Collection

Electron diffraction datasets from separate crystals were collected using an FEI Tecnai F20 transmission electron microscope operated at 200 kV, with the objective aperture fully open to evenly illuminate an area extending beyond the sample and setting the

selected area aperture to closely match the size of the crystal. For each crystal of thickness 200–400 nm, the same 23° wedge was repeatedly collected up to five times by continuously rotating the stage from -12° to +11° (-38° to -15° for crystal 3) off its untilted orientation at a constant rate of 0.089° s^{-1} (Nannenga et al., 2014b). The rate of electron exposure was adjusted to 0.007 e^{-} $Å^{-2}$ s^{-1}, calibrated using a Faraday cage. The individual datasets, each consisting of 49–50 frames with exposure time 5.1 s were recorded at a camera length setting of 1.2 m, corresponding to an effective detector distance of 2.2 m. All diffraction images were acquired using a TVIPS TemCam-F416 CMOS camera and corrected to account for negative pixel values (Hattne et al., 2015, 2016) prior to further processing.

Data Reduction

Proteinase K data were indexed and integrated in $P4_32_12$ using MOSFLM (Leslie and Powell, 2007) through its graphical interface iMosflm (Battye et al., 2011). Wedges from six different crystals were merged by the order in which they were collected using AIMLESS (Evans and Murshudov, 2013), and the set of free reflections was copied from the molecular replacement search model, PDB entry 5i9s. Neither of these crystals yield a complete dataset on their own, but since proteinase K does not exhibit a pronounced preferred orientation, this produced five reasonably complete datasets, each comprised of frames with a similar degree of exposure. The choice between intensities derived from summation integration and profile fitting was left up to the optimization algorithm implemented in AIMLESS; in all cases this resulted in profile-fitted intensities being used. Relative *B*-factors were calculated between merged single-crystal datasets with SCALEIT from the CCP4 suite (Howell and Smith, 1992; Winn et al., 2011).

To quantify the global effects of radiation damage, integrated intensities were averaged for each diffraction image. Averages from different crystals were scaled by a single factor in the range [0.10, 1.0] and simultaneously fit to a common function on the form $A \times \exp(-B \times x)$ using the BFGS minimizer implemented in scipy (Oliphant, 2007). The mean effective resolution was calculated by EFRESOL (Urzhumtseva et al., 2013) and used as an objective high-resolution cutoff for all datasets.

Phasing and Model Refinement

The first dataset was phased by molecular replacement using MOLREP (Vagin and Teplyakov, 1997) from PDB entry 5i9s, and the solution was reused for all subsequent datasets. Water molecules and ions were excluded from the refined structure: while these improve the quality of the model at high resolution, they are difficult to reliably model once damage degrades the quality of the data. This model was also used to calculate solvent-accessible areas with AREAIMOL (Winn et al., 2011).

All models were refined with REFMAC (Murshudov et al., 2011), with electron scattering factors calculated using the Mott–Bethe formula. The occupancies were set to unity for all atoms and no alternate confirmations were used to model partial damage to specific sites of the molecule. Further processing and refinement statistics are given in Table 1.

GSNQNNF

Crystal Growth

The 7-residue peptide GSNQNNF (>98% purity) was purchased from GenScript, dissolved in water at 10 mg ml^{-1}, and crystallized by the hanging-drop method in a high-throughput screen. Crystals grew as needle clusters at a 1:1 ratio of peptide solution to mother liquor in a condition containing 10% (w/v) PEG-8000, 0.1 M MES pH 6.0, and $Zn(OAc)_2$ (Martynowycz et al., 2017).

Sample Preparation

Clusters were broken by pipetting and dispensed onto glow-discharged grids, which were then blotted for 20 s and vitrified with force position 24. Otherwise, GSNQNNF samples were prepared identically to those of proteinase K.

Data Collection

Crystals of the hepta-peptide that were 100–500 nm thick, were tilted over ~60° at a three-fold higher rotation rate (0.3°s^{-1}) than was used for proteinase K and up to 12 sweeps were collected from each crystal. To probe the effect of dose rate on radiation damage, peptide data were collected at both 0.0028 e^{-} $Å^{-2}$ s^{-1} and 0.0017 e^{-} $Å^{-2}$ s^{-1}. These rates were tuned to maximize the number of sweeps collected from an individual crystal. Single crystal datasets comprised of approximately 100 images were collected with an exposure time of 2.1 s and camera length 0.73 m which corresponds to an effective sample to detector distance of 1.2 m. Because two orders of magnitude fewer reflections are typically observed on a diffraction pattern from short segments like GSNQNNF than from proteinase K, intensities were integrated with a higher gain value and averaged for each dataset instead of for each frame when estimating the effects of global damage on the hepta-peptide. Otherwise data collection was performed as detailed for proteinase K.

Data Reduction, Phasing, and Model Refinement

The datasets were indexed and integrated in *P*1 with XDS (Kabsch, 2010b) and an isomorphous subset was scaled and merged with XSCALE (Kabsch, 2010a). Phases for the GSNQNNF data were determined *ab initio* by direct methods from the first collected data set using SHELXD (Sheldrick, 2008). XDSCONV (Kabsch, 2010b) was used on this dataset to assign a free set of reflections, which was subsequently reused for all later peptide datasets. A ligated acetate, three water molecules, and a single zinc atom were included with the GSNQNNF model, because they constitute a significant fraction of the unit cell contents, and all atoms were fixed at full occupancy. Otherwise processing was performed as detailed for proteinase K; statistics for the datasets at the high and low dose rates are given in Tables 2 and 3, respectively.

QUANTIFICATION AND STATISTICAL ANALYSIS

Quantification and statistical analyses are given in Tables 1, 2, and 3. These values were extracted from the programs used to merge and refine the respective multi-crystal datasets.

DATA AND SOFTWARE AVAILABILITY

The atomic coordinates have been deposited in the Protein Data Bank under ID codes 6cl7 to 6clt. Density maps have been deposited in the Electron Microscopy Data Bank under ID codes EMD-7490 to EMD-7512.